Designing and Analyzing Sensor and Actuator of a Nano/Micro-System for Fatigue and Fracture Characterization of Nanomaterials

Mohammad Reza Zamani Kouhpanji

Abstract—This paper presents a MEMS/NEMS device for fatigue and fracture characterization of nanomaterials. This device can apply static loads, cyclic loads, and their combinations in nanomechanical experiments. It is based on the electromagnetic force induced between paired parallel wires carrying electrical currents. Using this concept, the actuator and sensor parts of the device were designed and analyzed while considering the practical limitations. Since the PWCC device only uses two wires for actuation part and sensing part, its fabrication process is extremely easier than the available MEMS/NEMS devices. The total gain and phase shift of the MEMS/NEMS device were calculated and investigated. Furthermore, the maximum gain and sensitivity of the MEMS/NEMS device were studied to demonstrate the capability and usability of the device for wide range of nanomaterials samples. This device can be readily integrated into SEM/TEM instruments to provide real time study of the mechanical behaviors of nanomaterials as well as their fatigue and fracture properties, softening or hardening behaviors, and initiation and propagation of nanocracks.

Keywords—Sensors and actuators, MEMS/NEMS devices, fatigue and fracture nanomechanical testing device, static and cyclic nanomechanical testing device.

I. INTRODUCTION

THE especial geometry and high surface to volume ratio of 1D nanomaterials as well as 2D nanomaterials, these nanostructures exhibit superior quantum confinement effects and high mobilities of carriers which make them excellent building blocks for electronics, phononics, and photonics devices [1]-[4]. These nanostructures are fundamental building blocks for a broad spectrum of nanotechnology applications including ultrahigh sensitive sensors and actuators [5], [6]; energy harvesting and storage [7], [8]; selective nanomaterial sieving [9], flexible electronics [10], [11]; and nanostructured light emitters [12], [13]. The quantum efficiency of these nanodevices drastically depends on their mechanical performance. That is why these nanodevices are continuously under the cyclic mechanical loadings induced by thermal stresses/strains, boundary conditions, quantum strains/stresses in addition to the residual stresses/strains due to lattice mismatches and partial fractures that may happen during the fabrication processes. These strains/stresses significantly reduce the quantum efficiency of the nanodevices by reducing the mobilities of the carriers and making nonhomogeneous

distributions of the carriers in the active region, and eventually causing the failure of nanodevices [14], [15].

The mechanical properties of 1D and 2D nanomaterials have been inspected using nanoindentations, uniaxial tensile tests, uniaxial compression tests, bending tests, and in situ SEM/TEM resonance techniques [16]-[18]. These techniques only provide the mechanical properties of the nanomaterials under static loadings. Consequently, to study the fatigue and fracture properties of the nanomaterials, the *in-situ* SEM/TEM fracture experiments were developed [19]-[22]. These techniques use a nanomanipulator to apply a static force on the nanomaterials until it breaks, where the fracture surface is analyzed to predict the fracture properties of the nanomaterials. These techniques provide a comprehensive information about the maximum stress/strain before fracture in addition to the nanomaterials behaviors in fracture. However, these techniques do not provide any information regarding to the softening or hardening behaviors of nanomaterials prior to fracture, the hysteresis behaviors of the nanomaterials as well as the propagation of the nano-cracks inside them.

The limitations of the in-situ nanomechanical testing resulted in a few attempts to implement the MEMS/NEMS devices for fatigue and fracture experiments [23], [24]. These MEMS/NEMS devices consist of two main parts, actuation part and sensing part. The most common used actuators are electrothermal actuators, electrostatic actuators, magnetic-based actuators, and piezoelectric-based actuators [25]. Among all these types of actuators, the electrothermal and electrostatic actuators have been widely used in nanomechanical testing MEMS/NEMS device because their simple fabrication and repeatable behaviors. Even though the unbounded growing demands of the nanomechanical testing techniques resulted in impressive development of the MEMS/NEMS devices, they are still suffering from several issues that limit their performance and applications. For example, due to the attractive forces between the combs of electrostatic actuators and their substrate, they cannot be driven at high voltages/currents [26], [27]. This limitation causes the electrostatic actuators to generate much smaller forces comparing to other types of MEMS/NEMS devices, especially the electrothermal actuators [28]. However, an alternative is to increase the number of the combs which increases the size of the MEMS/NEMS devices and complexities. Furthermore, the electrostatic actuators require complex flexible structures for generating large displacements resulting in structural nonlinearities [26], [29]. In contrast to

Mohammad Reza Zamani Kouhpanji is with the Electrical and Computer Engineering Department, University of Minnesota-Twin Cities, Minneapolis, MN 55455, USA (phone: +1(618)-305-9636; e-mail: mrzamani@unm.edu).

World Academy of Science, Engineering and Technology
International Journal of Mechanical and Materials Engineering
Vol:11, No:10, 2017

the electrostatic actuators, the electrothermal actuators do not suffer from these limitations. However, they generate large displacements in the costs of high power consumptions [30]. In addition to the difficulties for controlling the temperature of the samples during the experiment, the electrothermal actuators cannot be used at the cryogenic temperatures. More importantly, these MEMS/NEMS devices cannot apply fast, linear, and fully reversible cyclic loadings or their combinations with static loadings. The limitations of the nanomechanical testing techniques and MEMS/NEMS devices caused a huge gap between the characterizations of the nanomaterials under static loadings, cyclic loadings, and their combinations.

To fill this gap, here a MEMS/NEMS device for fatigue and fracture characterizations of nanomaterials under combinations of loadings is proposed and analyzed. This device is based on the paired wires carrying currents (PWCC) concept, which states that two parallel wires carrying currents exert force on each other due to their magnetic fields. This physics concept was implemented to design and analyse the actuator part and sensor part of the PWCC device, which drastically reduce the complexity of the actuator part and

sensor part resulting in ceasing the fabrication and characterization of the PWCC device.

II. DESIGN AND ANALYSIS

Fig. 1 shows the proposed structure for the PWCC device. The currents passing through the wire 1 and 2 generate a magnetic field surrounding them. This magnetic field results in an attractive or repulsive force applying on the wires 1 and 2 depending on their currents relative directions. The wires 1 and 2 act as the actuator for this PWCC device to generate a force/displacement on the wire 3, which can either be a 1D or 2D nanomaterials samples for testing. The wire 3 is connected to the wire 4, which leads the wire 4 to start moving in the magnetic field generated by the wire 5. Movement of the wire 4 in the magnetic field of the wire 5 generates a current in the wire 4, which can be detected and analyzed to understand the mechanical properties of the nanomaterials samples. The proposed PWCC device includes four parts; actuation part (wires 1 and 2), mechanical structure (wires 2, 3 and 4), sensing part (wires 4 and 5), and electrical circuit for measuring the sensor output.
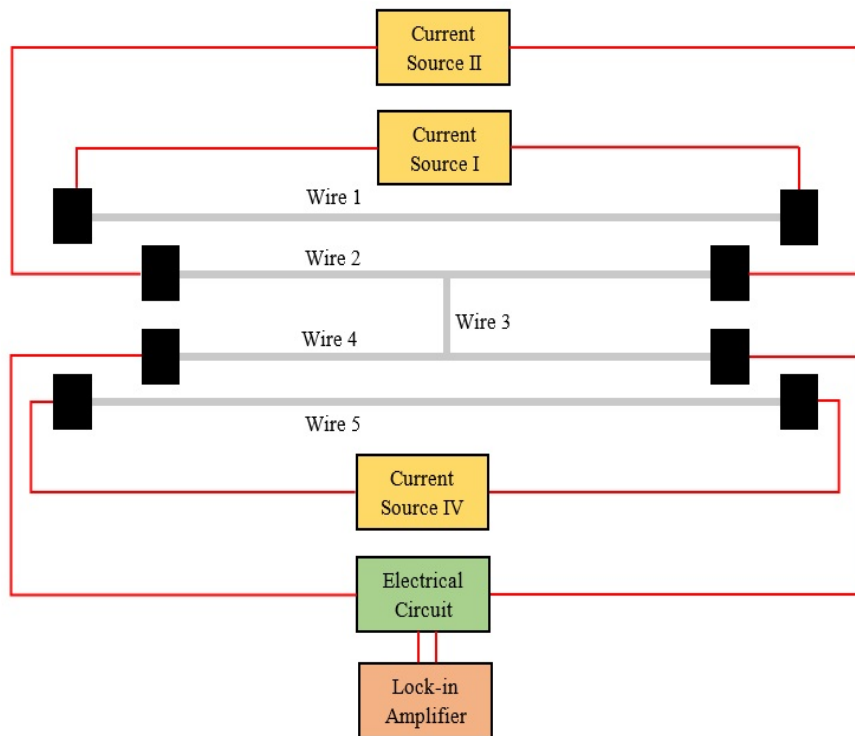

Fig. 1 The PWCC device and its proposed setup for nanomechanical cyclic testing

A. Actuation Part (Wires 1 and 2)

The wires 1 and 2 are connected to the current sources I and II carrying currents $i_1=c_1sin(\omega_1t)$ and $i_2=c_2sin(\omega_2t)$, respectively, as shown in Fig. 1. Fig. 2 shows the wires 1 and 2 cross view, which assumed to be in the y-z plane along the y-axis. The cross-sections of the wires considered rectangular shape to be consistent with the MEMS/NEMS fabrication

processes.

Since the wires lengths are much larger than the wires cross-sections and the distance between them, the wires are assumed to be infinite. Therefore, the magnetic field of each element of the wire 1, like point $P(x,y)$, at point $P_0(x_0,z_0)$ of the wire 2 can be written using Biot-Savart-Laplace law as [31]

World Academy of Science, Engineering and Technology
International Journal of Mechanical and Materials Engineering
Vol:11, No:10, 2017

$$dH_x(x_0, z_0) = \frac{2i_1}{cA_1} \frac{z_0 - z}{(x_0 - x)^2 + (z_0 - z)^2} dxdz$$

$$dH_z(x_0, z_0) = -\frac{2i_1}{cA_1} \frac{x_0 - x}{(x_0 - x)^2 + (z_0 - z)^2} dxdz$$

(1)

where, A_1 is the cross-section of the wire 1; and c is the light velocity. Since the wires lengths were assumed to be infinitive, the magnetic field in y-direction is zero. Taking integral over the wire 1 cross-section, the magnetic fields components are achieved as follows

$$H_x(x_0, z_0) = \frac{i_1}{cA_1} \left\{ \left[\begin{array}{c} \left(x_0 + \frac{w_1}{2}\right)\ln\left(1 + \frac{h_1 + 2z_0}{\left(x_0 + \frac{w_1}{2}\right)^2 + z_0^2} h_1\right) \\ +2(z_0 + h_1)\arctan\left(\frac{x_0 + \frac{w_1}{2}}{z_0 + h_1}\right) - 2z_0\arctan\left(\frac{x_0 + \frac{w_1}{2}}{z_0}\right) \end{array} \right] - \left[\begin{array}{c} \left(x_0 - \frac{w_1}{2}\right)\ln\left(1 + \frac{h_1 + 2z_0}{\left(x_0 - \frac{w_1}{2}\right)^2 + z_0^2} h_1\right) \\ +2(z_0 + h_1)\arctan\left(\frac{x_0 - \frac{w_1}{2}}{z_0 + h_1}\right) - 2z_0\arctan\left(\frac{x_0 - \frac{w_1}{2}}{z_0}\right) \end{array} \right] \right\}$$

(2)

$$H_z(x_0, z_0) = \frac{i_1}{cA_1} \left\{ \left[\begin{array}{c} z_0\ln\left(1 + \frac{\left(x_0 + \frac{w_1}{2}\right)^2}{z_0^2}\right) - (z_0 + h_1)\ln\left(1 + \frac{\left(x_0 + \frac{w_1}{2}\right)^2}{(z_0 + h_1)^2}\right) \\ -2\left(x_0 + \frac{w_1}{2}\right)\left(\arctan\left(\frac{z_0 + h_1}{x_0 + \frac{w_1}{2}}\right) - \arctan\left(\frac{z_0}{x_0 + \frac{w_1}{2}}\right)\right) \end{array} \right] - \left[\begin{array}{c} z_0\ln\left(1 + \frac{\left(x_0 - \frac{w_1}{2}\right)^2}{z_0^2}\right) - (z_0 + h_1)\ln\left(1 + \frac{\left(x_0 - \frac{w_1}{2}\right)^2}{(z_0 + h_1)^2}\right) \\ -2\left(x_0 - \frac{w_1}{2}\right)\left(\arctan\left(\frac{z_0 + h_1}{x_0 - \frac{w_1}{2}}\right) - \arctan\left(\frac{z_0}{x_0 - \frac{w_1}{2}}\right)\right) \end{array} \right] \right\}$$

(3)

where, w_1 is the width of the wire 1; h_1 is the height of the wire 1. The direction of the magnetic field vector is not shown in Fig. 2 because it changes by the currents' direction; however, it is always perpendicular to the line connecting P to P_0, parallel to the shown red-dashed line in Fig. 2. Using the magnetic field components determined in (2) and (3), the force applied on the wire 2 by the wire 1 can be calculated using Lorentz Law as

$$\vec{F}_{12} = \mu_0 \frac{i_1 i_2}{A_2} \left\{ \hat{x}\left[\int_{r_{12}+h_1}^{r_{12}+h_1+h_2} \int_{-w_2/2}^{w_2/2} H_z(x_0, z_0) dx_0 dz_0 \right] - \hat{z}\left[\int_{r_{12}+h_1}^{r_{12}+h_1+h_2} \int_{-w_2/2}^{w_2/2} H_x(x_0, z_0) dx_0 dz_0 \right] \right\}$$

(4)

Here, r_{12} is the distance between the wires 1 and 2 as shown in Fig. 2. According to (4), the force per unit length applied on the wire 2 has components in x- and z- directions. It can be readily shown that the force in x-direction is zero due to the symmetric geometry of the wires. Furthermore, the same force applied on the wire 2 is applied on the wire 1 as well. To avoid the vibration of the wire 1, the wire 1 is assumed to be thicker than the wire 2.

The transfer function of the actuation part of the PWCC device was defined to be the ratio of the force in z-direction to the applied currents in the Laplace domain. Therefore,

$$G_{Actuator} \equiv \frac{F_z}{I_{12}} = -\frac{\mu_0}{A_2} \int_{r_{12}+h_1}^{r_{12}+h_1+h_2} \int_{-w_2/2}^{w_2/2} H_x(x_0, z_0) dx_0 dz_0$$

(5)

where, I_{12} is the Laplace transfer of the product of the i_1 and i_2 currents, and F_z is the z-component of the force $\vec{F}_{12}$.
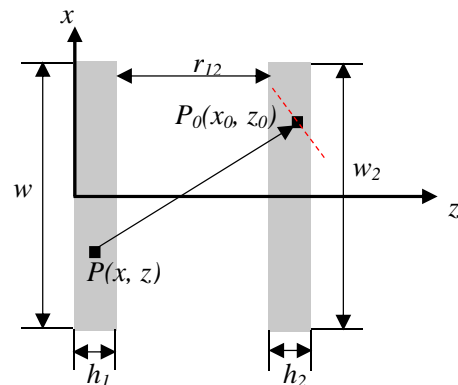

Fig. 2 Cross-section of the wires 1 and 2 contributing as actuator part for the PWCC device

C. Mechanical Structure (Wires 2, 3, and 4)

To simplify the structural analysis of the PWCC device, the technique of the parallel and series springs/dampers was

World Academy of Science, Engineering and Technology
International Journal of Mechanical and Materials Engineering
Vol:11, No:10, 2017

implemented. The wires 3 and 4 are series to each other. That is why, considering a force or displacement applied at the point A, both wires face the same amount of force but different amount of displacements. Fig. 3 represents the structural simplification flowchart of the PWCC device. The equivalent spring and damper constants of the wires 3 and 4 are shown in Fig. 3 (b) with K_{34} and λ_{34}, respectively. The wire 2 is parallel to the equivalent wire of the wires 3 and 4. Therefore,

$$K = K_2 + K_{34}, \qquad K_{34} = \left(\frac{1}{K_4} + \frac{1}{K_3} \right)^{-1},$$

$$\lambda = \lambda_2 + \lambda_{34}, \qquad \lambda_{34} = \left(\frac{1}{\lambda_4} + \frac{1}{\lambda_3} \right)^{-1} \qquad (6)$$

$$K_2 = \frac{384 E_2 I_2}{L_2^3}, \qquad K_4 = \frac{192 E_4 I_4}{L_4^3}, \qquad K_3 = \frac{E_3 A_3}{L_3}$$

where, E_i (i=2,3,4) is the Young's modulus of the wires; L_i (i=2,3,4) is the length of the wires; and I_i (i=2,3,4) is the second moments of the area of the wires. The total mass of the structure is considered equal to the mass of wire 2, $M=M_2$, where the masses of the other wires are ignored comparing to the mass of wire 2. This assumption was made to simplify the dynamic equations of the system by reducing the degrees of freedom from three to one. The impact of this assumption will be evaluated in the future works. However, in practical applications, since the wire III is a nanowire or nanomembrane, its mass is drastically smaller than the masses of wires II and IV. Therefore, the equivalent structure of the PWCC device, as shown in Figs. 3 (a) and (d), can be modeled as a mass connected to a spring and damper under a harmonic force, which is a well-known problem in dynamics mechanics with the following transfer function.
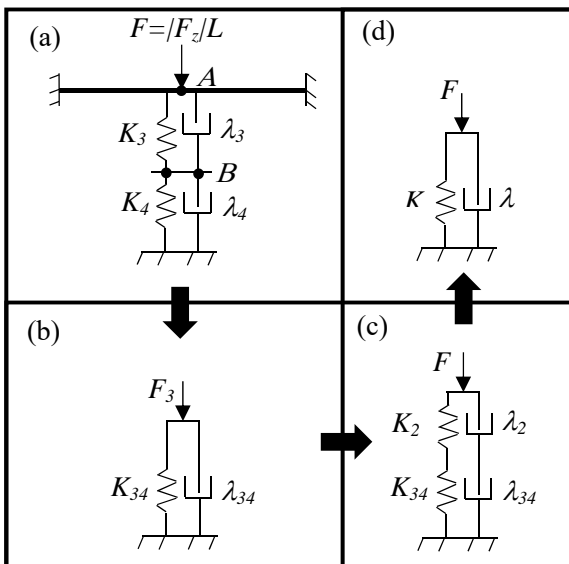

Fig. 3 Mechanical modeling of the PWCC device

$$G_A \equiv \frac{Z}{F_z} = \frac{1}{M} \frac{1}{s^2 + 2\zeta_m \omega_n s + \omega_n^2} \qquad (7)$$

ω_n is the resonance frequency of the system, $\sqrt{K/M}$; ζ_m is the mechanical damping ratio of the system, $\lambda / 2\sqrt{KM}$; K is the equivalent spring constant; and λ is the equivalent damping coefficient.

Equation (7) gives the transfer function of the maximum deflection at the point A. Implementing the concept of the parallel and series springs/dampers, the transfer function of the maximum deflection of the point B, which is at the center of the wire 4, can be found as

$$G_{Structural} = \frac{K_{34}}{K_4 M} \frac{1}{s^2 + 2\zeta_m \omega_n s + \omega_n^2} \qquad (8)$$

Equation (8) provides the motion of the center of the wire 4. It should be mentioned, according to [32], [33], the displacement of each point along wire 4 can be determined by multiplying its time response (determined by conducting the integral convolution of the Laplace inverses of transfer functions at (5) and (8)) and its eigenfunction. The eigenfunction of a continuous beam under clamped-clamped boundary condition, $\psi(y)$, is [33]

$$\psi(y) = \left\{ \begin{array}{l} \cosh\left(S_n \frac{y}{L_4} \right) - \cos\left(S_n \frac{y}{L_4} \right) \\ - \frac{\cosh(S_n) - \cos(S_n)}{\sinh(S_n) - \sin(S_n)} \left(\sinh\left(S_n \frac{y}{L_4} \right) - \sin\left(S_n \frac{y}{L_4} \right) \right) \end{array} \right\} \qquad (9)$$

Here, S_n corresponds to the mode of resonant of the wire 4, which are the solutions of $cosh(S_n)cos(S_n)=1$.

D. Sensing Part (Wires 4 and 5)

The wires 4 and 5 work as the sensing part of the PWCC device. The wire 5 is connected to a current source, shown as current source IV in Fig. 1, carrying the current i_5. This current generates a magnetic field around the wire 5 which can be calculated similar to (2) and (3), where the coefficients i_1/A_1 must be replaced by i_5/A_5, A_5 is the cross-section area of the wire 5. According to Faraday's Law, because the wire 4 is moving in the magnetic field of the wire 5 with a known velocity, an electric potential is induced between its two ends [34]. The transfer function for the induced potential can be determined as

$$G_{Sensor} \equiv \frac{\Delta V_4}{Iv} = \frac{1}{\psi\left(\frac{L_4}{2} \right) A_4} \int_0^{L_4} \psi(y) dy \int_0^{h_4} \int_{-w_4/2}^{w_4/2} H_x dx_0 dz_0 \qquad (10)$$

where, Iv is the Laplace transfer of the product of the current flowing in the wire 5 and velocity of each point along wire 4; ΔV_4 is the Laplace of the induced voltage between the two ends of the wire 4; A_4 is the cross-section area of the wire 4; and $\psi(L_4/2)$ is the value of the eigenfunction at the center of the wire 4. Since the velocity is the time derivative of the displacement, thus the transfer function from displacement to

World Academy of Science, Engineering and Technology
International Journal of Mechanical and Materials Engineering
Vol:11, No:10, 2017

velocity of the point B is

$$G_{Velocity} = s \qquad (11)$$

In practical applications, in order to detect the induced voltage, it is necessary to design a circuit to amplify the induced voltage and filter all noises before sending it to a lock-in amplifier for measuring. Since the purpose of this work is to prove the concept of the PWCC devices for future

applications, a simple bandpass and amplifying circuit is considered and analyzed. However, in the practical applications, it may need to implement several blocks of this circuit in series. Fig. 4 shows a simple state variable filter operated as a bandpass filter followed by an inverting operational amplifier. The state variable filter was suggested for the PWCC device because it provides ultrahigh quality factor (Q-factor) which can be set independent of its gain and its cut-off frequency of the filter [35], [36].
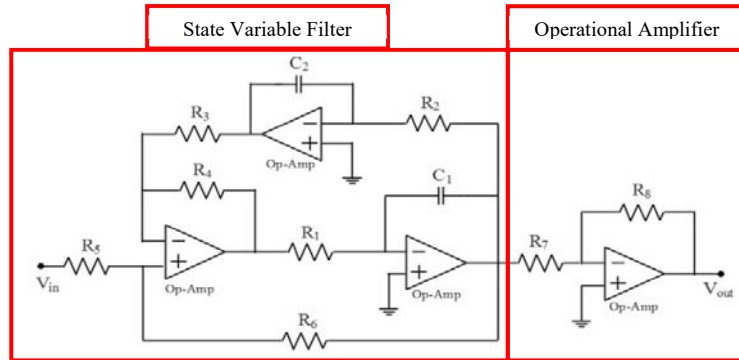

Fig. 4 Electrical circuit including a state variable filter operating as bandpass filter followed by an operational amplified

The transfer function of the electrical circuit at Fig. 4 can be determined as

$$G_{Electrical}(s) = \frac{a_0 s}{s^2 + a_1 s + a_2}, a_0 = \frac{R_8 R_6}{R_7 R_5} \frac{1}{R_1 C_1} \frac{1 + R_4/R_3}{1 + R_6/R_5},$$

$$a_1 = \frac{1}{R_1 C_1} \frac{1 + R_4/R_3}{1 + R_6/R_5}, \quad a_2 = \frac{R_4}{R_3} \frac{1}{R_1 C_1 R_2 C_2} \qquad (12)$$
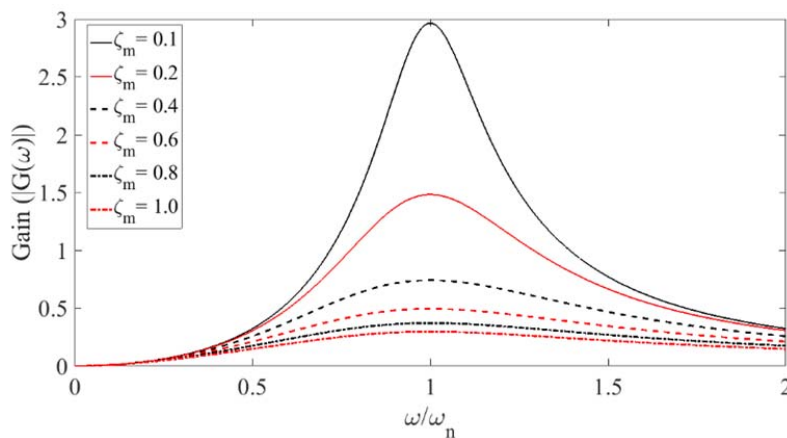
where, R_i (i=1,2,...,8) are the resistors; C_i (i=1,2) are the capacitors; V_{in} is the induced voltage at the wire 4 equal to ΔV_4; V_{out} is the output signal after implementing bandpass

filter and amplifying the input voltage. The total added gain by this circuit is proportional to the R_8/R_7 and R_6/R_5. The ratio R_8/R_7 is the gain added by the operational amplifier, as shown in Fig. 4. Also, the ratio R_6/R_5 is the gain added by the state variable filter, and it is proportional to its Q-factor, which can be adjusted to make it ultranarrow bandwidth to be highly selective.
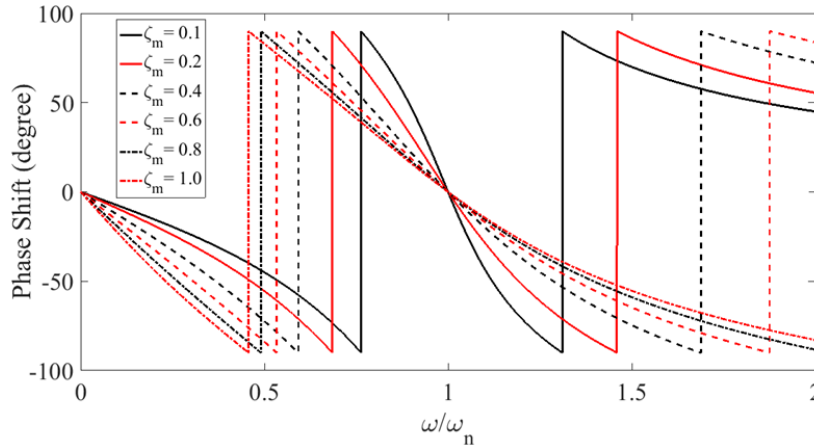
III. RESULTS AND DISCUSSIONS

The total transfer function of the PWCC device is the product of the all transfer functions as

$$G(s) = G_{Actuator} \ G_{Structural} \ G_{Velocity} \ G_{Sensor} \ G_{Electrical} \qquad (13)$$

(a) The total gain of the PWCC device

World Academy of Science, Engineering and Technology
International Journal of Mechanical and Materials Engineering
Vol:11, No:10, 2017

(b) The total phase shift of the PWCC device

Fig. 5 Total gain and phase shift of the PWCC device vs. the frequency for different mechanical damping ratios

The total gain and the phase shift of the PWCC device are plotted in Fig. 5 for different mechanical damping ratios. To achieve the highest gain, the resonance frequency of the electrical circuit was designed to be the same as the resonance frequency of the mechanical structure of the PWCC device by choosing the appropriate capacitors 1 and 2 as well as resistors 1 and 2.
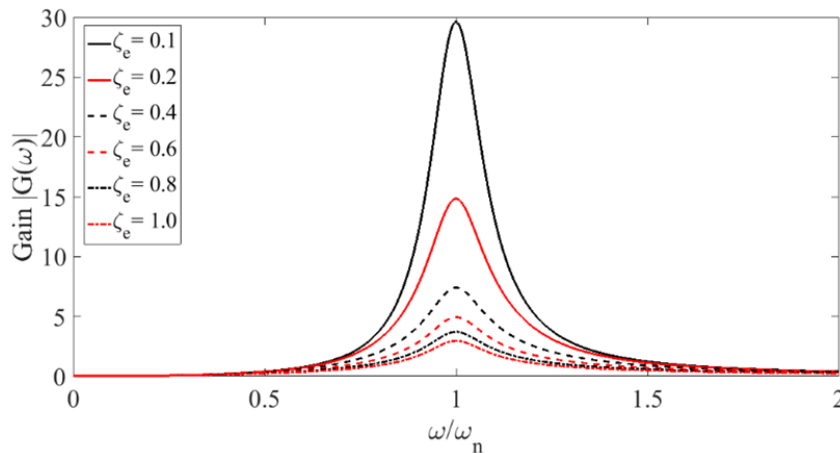
For some applications, it may be necessary to implement the currents 1, 2, and 5 at different frequencies. In these cases, the most general form of the time dependent part of the PWCC device response will have the following terms

$$
\begin{aligned}
&\frac{d}{dt}\left[\sin(\omega_1 t)\sin(\omega_2 t)\right]\sin(\omega_5 t) \\
&= \left\{ \begin{array}{l} \omega_1 \cos(\omega_1 t)\sin(\omega_2 t)\sin(\omega_5 t) \\ + \omega_2 \sin(\omega_1 t)\cos(\omega_2 t)\sin(\omega_5 t) \end{array} \right\} \\
&= \left\{ \begin{array}{l} \dfrac{\omega_1}{4}\left[\begin{array}{l} \cos((\omega_1+\omega_2-\omega_5)t)-\cos((\omega_1+\omega_2+\omega_5)t) \\ +\cos((\omega_2-\omega_1-\omega_5)t)-\cos((\omega_2-\omega_1+\omega_5)t) \end{array} \right] \\ +\dfrac{\omega_2}{4}\left[\begin{array}{l} \cos((\omega_1+\omega_2-\omega_5)t)-\cos((\omega_1+\omega_2+\omega_5)t) \\ +\cos((\omega_1-\omega_2-\omega_5)t)-\cos((\omega_1-\omega_2+\omega_5)t) \end{array} \right] \end{array} \right\}
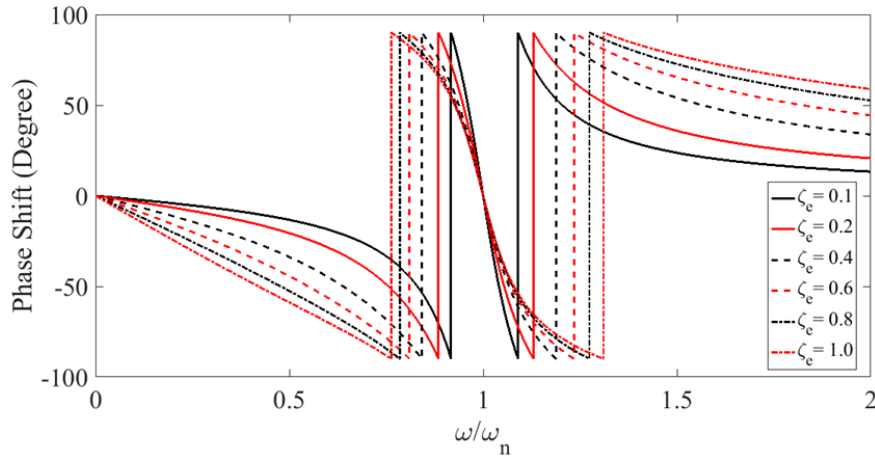\end{aligned}
\tag{14}
$$

According to (14), the response of the PWCC device oscillates at four different frequencies. Therefore, the electrical circuit must have high Q-factor, equivalently very small electrical damping ratio $(\zeta_e = \frac{1}{2Q} = \frac{a_1}{2\sqrt{a_2}})$ to precisely detect the signal at the desired frequency. To study the effects of the electrical damping ratio, Fig. 6 was prepared to render the total gain and the phase shift of the PWCC device for different electrical damping ratios.

The total gain and phase shift of the PWCC device have the same behaviors in terms of the mechanical and electrical damping ratios. According to both Figs. 5 and 6, as the mechanical/electrical damping ratio increases, the maximum gain decreases. However, the PWCC device gain has more sensitivity with respect to the electrical damping ratio comparing to the mechanical damping ratio. Note that as the damping ratios decreases, the phase shift discontinuities approach toward the frequency resonance of the PWCC device, where the phase shift has the highest sensitivity.

(a) The total gain of the PWCC device

World Academy of Science, Engineering and Technology
International Journal of Mechanical and Materials Engineering
Vol:11, No:10, 2017

(b) The total phase shift of the PWCC device

Fig. 6 Total gain and phase shift of the PWCC device vs. the frequency for different electrical damping ratios
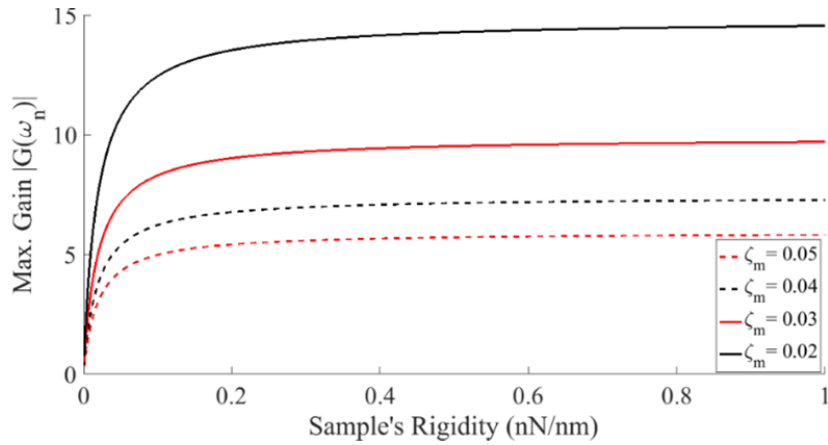

Fig. 7 Maximum gain of the PWCC device in terms of the sample's rigidity. The wire 3 is the place where the sample is
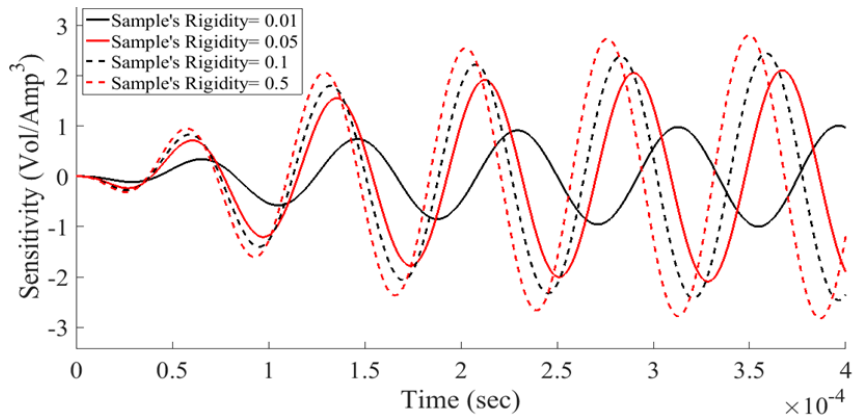

Fig. 8 The sensitivity of the PWCC device

For successfully designing any MEMS/NEMS device for nanomechanical testing, analyzing the maximum gain and time-domain response sensitivity of the MEMS/NEMS device in terms of the mechanical properties of the sample, which is connected to the wires 2 and 4 instead of the wire 3, carries a crucial role on the performance of the MEMS/NEMS device. Fig. 7 shows the maximum gain of the PWCC device in terms of the sample rigidity. As it can be seen, the maximum gain increases as the rigidity of the sample increases. Moreover, the maximum gain is almost independent of the rigidity of the sample with large rigidities.

Regardless of the vicinity of the zero rigidity that the maximum gain approaches to zero, the PWCC device gain monotonically increases as the sample's rigidity increases

World Academy of Science, Engineering and Technology
International Journal of Mechanical and Materials Engineering
Vol:11, No:10, 2017

toward infinity, which proves the applicability of the PWCC device for a wide range of sample sizes and materials.

The time-domain response sensitivity of the PWCC device can be calculated

$$\text{Sensitivity} = \frac{d}{dI}(\Delta V) \qquad (15)$$

where, I is the product of the all input currents amplitudes ($|i_1 i_2 i_5|$); ΔV is the induced voltage between two ends of the wire 4 in time space. Fig. 8 shows the sensitivity of the PWCC device, which can be used to understand the transient and steady state responses of the PWCC device. The sensitivity analysis shows that the PWCC device has higher sensitivities for samples with larger rigidities. Furthermore, as the sample rigidity increases, the phase shift of the response slowly increases and it approaches to π phase shift.

IV. CONCLUSION

This study represents a PWCC device for nanomechanical testing applications which can apply static loads, cyclic loads, and their combinations. The total gain and phase shift of the PWCC device were investigated. The total gain and phase shift of the PWCC device are very sensitive to the electrical damping ratio of the device comparing to the mechanical damping ratio of the device. The phase shift discontinuities happen at vicinity of the resonance frequency of the device, and they become closer to each other as the damping ratios decrease. The maximum gain of the PWCC device increases as the rigidity of the sample increases, which proves the capability of the device for a broad range of samples. From analyzing the sensitivity of the PWCC device, it can be concluded that phase shift dependency of the PWCC device slowly changes as the sample rigidity approaches the large values.

REFERENCES

[1] Fiori G, Bonaccorso F, Iannaccone G, Palacios T, Neumaier D, Seabaugh A, Banerjee SK, Colombo L. Electronics based on two-dimensional materials. Nature nanotechnology. 2014 Oct 1;9(10):768-79.

[2] Zamiri M, Anwar F, Klein BA, Rasoulof A, Dawson NM, Schuler-Sandy T, Deneke CF, Ferreira SO, Cavallo F, Krishna S. Antimonide-based membranes synthesis integration and strain engineering. Proceedings of the National Academy of Sciences. 2016 Dec 16;201615645.

[3] Goldberger J, He R, Zhang Y, Lee S. Single-crystal gallium nitride nanotubes. Nature. 2003 Apr 10;422(6932):599.

[4] Patolsky F, Timko BP, Yu G, Fang Y, Greytak AB, Zheng G, Lieber CM. Detection, stimulation, and inhibition of neuronal signals with high-density nanowire transistor arrays. Science. 2006 Aug 25;313(5790):1100-4.

[5] Li W, Xu H, Zhai T, Yu H, Chen Z, Qiu Z, Song X, Wang J, Cao B. Enhanced triethylamine sensing properties by designing Au@ SnO 2/MoS 2 nanostructure directly on alumina tubes. Sensors and Actuators B: Chemical. 2017 Jun 3.

[6] Patil VL, Vanalakar SA, Patil PS, Kim JH. Fabrication of nanostructured ZnO thin films based NO 2 gas sensor via SILAR technique. Sensors and Actuators B: Chemical. 2017 Feb 28;239:1185-93.

[7] Liu XH, Wang JW, Huang S, Fan F, Huang X, Liu Y, Krylyuk S, Yoo J, Dayeh SA, Davydov AV, Mao SX. In situ atomic-scale imaging of electrochemical lithiation in silicon. Nature nanotechnology. 2012 Nov 1;7(11):749-56.

[8] Wang ZL, Song J. Piezoelectric nanogenerators based on zinc oxide nanowire arrays. Science. 2006 Apr 14;312(5771):242-6.

[9] Koenig SP, Wang L, Pellegrino J, Bunch JS. Selective molecular sieving through porous graphene. Nature nanotechnology. 2012 Nov 1;7(11):728-32.

[10] Fan Z, Ho JC, Takahashi T, Yerushalmi R, Takei K, Ford AC, Chueh YL, Javey A. Toward the development of printable nanowire electronics and sensors. Advanced Materials. 2009 Oct 5;21(37):3730-43.

[11] McAlpine MC, Friedman RS, Jin S, Lin KH, Wang WU, Lieber CM. High-performance nanowire electronics and photonics on glass and plastic substrates. Nano Letters. 2003 Nov 12;3(11):1531-5.

[12] Hong YJ, Lee CH, Yoon A, Kim M, Seong HK, Chung HJ, Sone C, Park YJ, Yi GC. Visible-color-tunable light-emitting diodes. Advanced Materials. 2011 Aug 2;23(29):3284-8.

[13] Li C, Wright JB, Liu S, Lu P, Figiel JJ, Leung B, Chow WW, Brener I, Koleske DD, Luk TS, Feezell DF. Nonpolar InGaN/GaN Core–Shell Single Nanowire Lasers. Nano letters. 2017 Jan 24;17(2):1049-55.

[14] Zamani Kouhpanji, MR. "Investigating the classical and non-classical mechanical properties of GaN nanowires." MS Thesis, University of New Mexico, Albuquerque, NM 87131, USA. (2017). http://digitalrepository.unm.edu/ece_etds/354

[15] Farsad E, Abbasi SP, Goodarzi A, Zabihi MS. Experimental parametric investigation of temperature effects on 60W-QCW diode laser. World Acad. Sci. Eng. Technol. 2011 Nov 28;59:1190-6.

[16] Zamani Kouhpanji MR, Jafaraghaei U. A semianalytical approach for determining the nonclassical mechanical properties of materials. arXiv preprint arXiv:1706.06559. 2017 Jun 20.

[17] Zhu Y, Chang TH. A review of microelectromechanical systems for nanoscale mechanical characterization. Journal of Micromechanics and Microengineering. 2015 Aug 19;25(9):093001.

[18] Treacy MJ, Ebbesen TW, Gibson JM. Exceptionally high Young's modulus observed for individual carbon nanotubes. Nature. 1996 Jun 20;381(6584):678.

[19] Zhang Y, Wang F, Zang P, Wang J, Mao S, Zhang X, Lu J. In-situ observation of crack propagation through the nucleation of nanoscale voids in ultra-thin, freestanding Ag films. Materials Science and Engineering: A. 2014 Nov 17;618:614-20.

[20] Lu Y, Song J, Huang JY, Lou J. Fracture of Sub-20nm Ultrathin Gold Nanowires. Advanced Functional Materials. 2011 Oct 21;21(20):3982-9.

[21] Agrawal R, Peng B, Espinosa HD. Experimental-computational investigation of ZnO nanowires strength and fracture. Nano letters. 2009 Sep 30;9(12):4177-83.

[22] Huang JY, Zheng H, Mao SX, Li Q, Wang GT. In situ nanomechanics of GaN nanowires. Nano letters. 2011 Mar 18;11(4):1618-22.

[23] Hosseinian E, Pierron ON. Quantitative in situ TEM tensile fatigue testing on nanocrystalline metallic ultrathin films. Nanoscale. 2013 Nov 22;5(24):12532-41.

[24] Kahn H, Ballarini R, Mullen RL, Heuer AH. Electrostatically actuated failure of microfabricated polysilicon fracture mechanics specimens. InProceedings of the royal society of london a: mathematical, physical and engineering sciences 1999 Oct 8 (Vol. 455, No. 1990, pp. 3807-3823). The Royal Society.

[25] Kheyraddini Mousavi A, Alaie S, Leseman ZC. Basic MEMS Actuators. Encyclopedia of Nanotechnology. 2016:1-6.

[26] Legtenberg R, Groeneveld AW, Elwenspoek M. Comb-drive actuators for large displacements. Journal of Micromechanics and microengineering. 1996 Sep;6(3):320.

[27] Pisano AP, Cho YH. Mechanical design issues in laterally-driven microstructures. Sensors and Actuators A: Physical. 1990 Apr 1;23(1-3):1060-4.

[28] Maloney JM, Schreiber DS, DeVoe DL. Large-force electrothermal linear micromotors. Journal of Micromechanics and Microengineering. 2003 Nov 17;14(2):226.

[29] Que L, Park JS, Gianchandani YB. Bent-beam electro-thermal actuators for high force applications. InMicro Electro Mechanical Systems, 1999. MEMS'99. Twelfth IEEE International Conference on 1999 Jan 21 (pp. 31-36). IEEE.

[30] Zhu Y, Corigliano A, Espinosa HD. A thermal actuator for nanoscale in situ microscopy testing: design and characterization. Journal of micromechanics and microengineering. 2006 Jan 5;16(2):242.

[31] Feynman RP, Leighton RB, Sands M. The Feynman Lectures on Physics, Desktop Edition Volume I. Basic books; 2013 Oct 31.

[32] Nayfeh AH Nonlinear Oscillation. New York: John Wiley and Sons, 1979.

[33] Kahrobaiyan MH, Asghari M, Hoore M, Ahmadian MT. Nonlinear size-

World Academy of Science, Engineering and Technology
International Journal of Mechanical and Materials Engineering
Vol:11, No:10, 2017

dependent forced vibrational behavior of microbeams based on a non-classical continuum theory. Journal of Vibration and Control. 2012 Apr;18(5):696-711.

[34] Nayfeh MH, Brussel MK. Electricity and magnetism. Courier Dover Publications; 2015 Feb 9.

[35] Derek Rowell. *2.161 Signal Processing: Continuous and Discrete*. Fall 2008. Massachusetts Institute of Technology: MIT OpenCourseWare, https://ocw.mit.edu. License: Creative Commons BY-NC-SA.

[36] Taylor FJ. State Variable Filter Models. Digital Filters: Principles and Applications with MATLAB.:183-96.